

Temperature and velocity determination of shock-heated flows with non-resonant heterodyne laser-induced thermal acoustics

F. J. Förster¹ · S. Baab¹ · G. Lamanna¹ · B. Weigand¹

Received: 13 July 2015 / Accepted: 1 September 2015 / Published online: 21 September 2015
© Springer-Verlag Berlin Heidelberg 2015

Abstract Non-resonant laser-induced thermal acoustics (LITA), a four-wave mixing technique, was applied to post-shock flows within a shock tube. Simultaneous single-shot determination of temperature, speed of sound and flow velocity behind incident and reflected shock waves at different pressure and temperature levels are presented. Measurements were performed non-intrusively and without any seeding. The paper describes the technique and outlines its advantages compared to more established laser-based methods with respect to the challenges of shock tube experiments. The experiments include argon and nitrogen as test gas at temperatures of up to 1000 K and pressures of up to 43 bar. The experimental data are compared to calculated values based on inviscid one-dimensional shock wave theory. The single-shot uncertainty of the technique is investigated for worst-case test conditions resulting in relative standard deviations of 1, 1.7 and 3.4 % for Mach number, speed of sound and temperature, respectively. For all further experimental conditions, calculated values stay well within the 95 % confidence intervals of the LITA measurement.

1 Introduction

The paper presents laser-induced thermal acoustics (LITA) as diagnostic tool for shock tube facilities. LITA combines a number of desirable features including non-intrusive, seedless point measurements of several flow properties.

Challenges arising from measurements in impulse facilities are briefly addressed followed by a discussion of LITA with respect to more established techniques. An overview of existing studies using LITA in shock-induced flows is given to clarify the resulting motivation of the presented work.

Shock tubes are widely used in a variety of scientific applications, which feature high pressure and temperature environments (e.g. shock-induced flows [1], combustion chemistry [2], fluid disintegration [3] and reentry physics [4]). However, quantitative measurements under such conditions are inherently challenging. In addition, the very short test duration requires fast-response techniques. Acquiring multiple gas properties from a single experiment is desirable as turn-around times and operational costs may be considerable.

Conventional probing techniques as employed in wind tunnels are intrusive, which make measurements inside the flow field difficult due to interference with the flow. Sensors embedded into the model or shock tube wall are commonly used to measure pressure. For temperature, this is more challenging as—in contrast to pressure—temperatures measured at the surface and inside the flow may differ significantly due to the boundary layer [5].

Laser-based techniques can potentially overcome all these problems. In addition to well-established techniques such as tunable diode laser absorption spectroscopy (TDLAS) [6, 7], laser-induced fluorescence (LIF) [8–10] or coherent anti-Stokes Raman spectroscopy (CARS) [11, 12], the authors evaluate LITA as a diagnostic tool for pulsed facilities. For temperature measurements after reflected shock waves similar to those used in this study, Farooq et al. [13] reported a relative standard deviation of 0.5 % for TDLAS. Furthermore, mean discrepancies to theoretical values of 3.6 % were found for LIF [9]. Precision

✉ F. J. Förster
felix.foerster@itlr.uni-stuttgart.de

¹ Institute of Aerospace Thermodynamics (ITLR), University of Stuttgart, Pfaffenwaldring 31, 70569 Stuttgart, Germany

of single-shot CARS measurements is assumed in the order of 3 % [14].

Like CARS, LITA is a four-wave mixing technique, but with the signal beam generated as a first-order Bragg scattering from a laser-induced grating. Two beams of a short-pulse, narrowband laser source (excitation or driver laser) are crossed to modulate the complex refraction index of the test medium in the measurement volume. This spatially periodic perturbation scatters light of a third input wave originating from a second laser source (interrogation or probe laser) into a fourth, coherent signal beam from which the physical properties of the test medium are derived. Originally observed as parasitic signal in degenerate four-wave mixing (DFWM) signals [15, 16], the temporal evolution of grating growth and decay has been treated theoretically by Cummings [17] and others [16, 18]. Since then, it has been demonstrated to measure speed of sound [19, 20] and temperature [21–23], transport properties [24–27], species concentration [28–30], pressure [31, 32] and flow velocity [33, 34].

In gas phases, the grating formation is dominated by two optoacoustic effects, namely electrostriction and thermalization. Rapid forcing of the test medium by the applied electric field results in two counter-propagating acoustic waves. If thermalization is present, an additional stationary thermal wave is generated. Light scattered from these structures resolves the temporal evolution of these waves as a function of the gas properties. The signal is a damped oscillation, whose frequency is proportional to the speed of sound. The decay rate and intensity are related to the transport properties—namely thermal diffusion and acoustic damping—as well as species concentration and pressure. In addition, LITA can be used for velocimetry as the scattered signal beam experiences a Doppler shift due to the flow velocity. The approach is similar to laser Doppler velocimetry (LDV), but with the induced grating as substitute for the seeding particles resulting in seedless Doppler velocimetry. In extension to homodyne detection, heterodyne mixing of the signal beam with a local oscillator allows to isolate this Doppler shift in the frequency domain.

LITA is a non-intrusive point measurement technique, where the measurement volume is defined by the overlap of the beams similar to CARS. Generally, several flow quantities are obtained simultaneously from a single-shot measurement. Focusing the input beams down to the measurement volume, CARS and LITA offer good spatial resolution. The capability of point measurements is advantageous compared to the line-of-sight averaged measurement found for TDLAS if inhomogeneous flows or flows with significant influence of boundary layers, e.g. small-diameter shock tubes [35], are investigated. On the other hand, data collection for spatial variations is tedious compared to LIF, which provides a planar measurement from a single

shot. Extension to one-dimensional measurements has been reported for CARS [36] and more recently for LITA [37] to reduce this drawback.

TDLAS, however, excels in temporal resolution by using rapidly tuned diode lasers. Repetition rates in the kHz [38] and MHz range [39] result in effectively continuous measurements. On the contrary, LIF, CARS and LITA are commonly restricted to single-shot measurements due to the repetition rate of the pulsed, high-power lasers, e.g. 10 Hz for Nd:YAG lasers. Megahertz pulse-burst lasers have been demonstrated for flow visualization [40] and velocimetry [41] applications to reach temporal resolutions comparable to TDLAS. Using short and ultra-short-pulse lasers, LIF (i.e. [42, 43]) and CARS (i.e. [44, 45]) measurements were presented with temporal resolutions in the kHz range. The lifetime of LITA signals is generally short enough to allow these repetition rates. Hence, LITA measurements are expected to benefit from such equipment in a similar way.

While TDLAS systems are relatively simple to implement, experimental setups for LIF, CARS and LITA are more complex. Among the latter, common laser and detection equipment is sufficient only for LITA. Here, the lasers can operate at a wide range of output wavelengths chosen independently from the test gas as gratings can be generated via electrostriction. Hence, there is no direct need for a tunable laser to access molecular absorption lines. Signal detectors can be fast photodiodes or photomultipliers instead of high-resolution spectrometer or low-noise, possibly intensified CCD cameras. Although LITA signal intensity boosts for near-resonant or resonant wavelengths [19], the paper shows that completely non-resonant signals are sufficient for the investigated conditions. This is important as, firstly, absolute measurements of species concentration may be found as ratio of resonantly and non-resonantly generated signals [28] similar to what was demonstrated by O'Byrne et al. for CARS [46]. Secondly, it shows that tracer molecules are also not required as seeding for LITA, which is usually the case for LIF [9, 47].

LITA further distinguishes from the other techniques, since a quantitative signal analysis is simpler. Excited-state populations and inter-molecular energy transfer govern the signal analysis for CARS and DFWM. Gas properties are derived from the shape and intensity of spectral features found by comparison of experimental and theoretical spectra. Quantum mechanical treatment of the susceptibility gratings makes the calculation of the theoretical spectra complex and time consuming, especially if multiple species are involved [48]. LITA gratings result as a small distortion of the bulk properties of the medium. Linearized hydrodynamics equations for the grating dynamics and light scattering are sufficient for an analytic expression of the LITA signals [17]. Detailed information of the spectroscopic properties of the test gas as to interpret spectral features is

not required—an advantage that also holds against LIF and TDLAS.

Furthermore, LITA excels if increased collisional quenching is present. While LITA signal intensities and lifetimes are enhanced, LIF signals, for instance, decrease as this enables a non-radiant return of excited molecules to ground state. As quantitative measurements from LIF signals also require the excitation dynamics and energy transfers to be modeled accurately, the contribution of quenching usually prevents an easy derivation of flow quantities. This and other effects including path-length absorption of excitation light, re-absorption of the fluorescence or tracer concentration must be addressed in a comprehensive calibration. LITA calibration, on the other hand, is straightforward as only the fringe spacing is required for quantitative measurements as detailed below.

A unique feature of LITA is that signal analysis can be conducted independently from the intensity. Flow velocity, speed of sound and—for known gas composition—temperature can be found solely from a frequency analysis of the time-resolved signal. This is especially advantageous if signal quality is low, for instance when the signal is strongly deteriorated by stray light or other negative influences of harsh environmental conditions. Examples for such are rocket nozzle flows [49], piston engines [50] or supersonic free jets [51].

These advantages motivate to pursue LITA as diagnostic tool, and so it has been already used to study shock-induced phenomena. Herring et al. [52] used non-resonant LITA to measure Mach number, speed of sound, temperature and pressure behind an oblique shock and expansion fan generated in a supersonic wind tunnel. Results were compared to Doppler global velocimetry (DGV) measurements and yielded excellent agreement, suggesting that LITA is viable for shock-strength measurements. Root mean square uncertainties for averages of 500 signals were found to be within 0.2, 0.4 and 4 % for Mach number, static temperature and pressure [31]. Due to the high flow velocity, measurements were taken at rather low temperatures and pressures ranging from 180 to 200 K and 7 to 8 kPa, respectively. Mizukaki et al. [53] used LITA to study temperature changes behind spherical shock waves generated by high-voltage discharges in air. Temperatures up to 380 K and the decay back to ambient conditions were measured with a maximum error of 5 %.

Sander et al. [54] used homodyne LITA in a shock tube at elevated temperatures and pressures. Their paper focuses on temperature measurements behind reflected shock waves using air as test gas. The incident shock Mach number was gradually increased leading to post-reflected shock pressures from 3.4 to 20 bar with corresponding temperatures of 440 K to 840 K. Most experiments were conducted with a NO₂ seeding to improve the signal quality. They found a

maximum error of 8 % between measured and theoretically predicted temperatures and a relative standard deviation of 3 % for selected test runs.

The presented paper differs from related work in such that a heterodyne detection scheme is used for simultaneous measurements of Mach number, speed of sound and temperature. Measurements were performed after both the incident and the reflected shock wave at different experimental conditions. As signal intensity increases with pressure, but strongly decreases with temperature [55], four temperature levels were investigated at different pressures to demonstrate the technique's potential. The accuracy and precision were evaluated for the worst-case condition of each flow regime. The complete experimental set includes temperatures and pressures ranging from 420 to 1000 K and 1 to 43 bar, respectively. For each condition, non-resonant LITA signals were sufficiently strong which allowed truly seedless measurements. In addition, the practicality of LITA is shown for two widely used test gases, namely nitrogen and argon. To the author's knowledge, this is the first time that non-resonant, heterodyne LITA is demonstrated for post-incident and reflected shock measurements obtaining several flow quantities from a single measurement.

2 Experimental facility and operating conditions

2.1 Shock tube

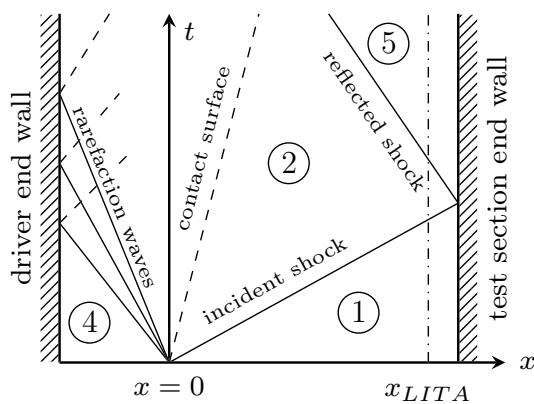
A double-diaphragm shock tube developed at the Institute of Aerospace Thermodynamics (ITLR) was used for the LITA measurements. The tube has an internal diameter of 72 mm with a 3.0-m-long driver section. The driven section is 9.4 m long. For improved optical accessibility, a transition from round cross-section to a square-shaped test section of 1 m length is realized with an intermediate piece (skimmer). The test section has an edge length of 50 mm and optical access is provided by 40-mm-thick quartz windows (Schott Lithosil TM Q1). The shock tube can provide test times of 2–5 ms with pressures of up to 50 bar and temperatures of 2000 K. A detailed characterization of the ITLR shock tube can be found in [56].

2.2 Shock tube operating conditions

Table 1 shows the 12 investigated nominal conditions. The portfolio comprises test gases argon (cases C1–C6) and nitrogen (C7–C12) at different flow conditions and pressure levels. To clarify the present flow characteristic, Fig. 1 schematically illustrates different states during an experiment via a location–time (x, t) plot in compliance with the conventional nomenclature. Given a fixed location for the

Table 1 Design conditions for LITA measurements

Case	Driver	Test gas	State	M_s (-)	p_{th} (bar)	T_{th} (K)
C1	He/Ar	Ar	2	1.96	2	600
C2	He/Ar	Ar	2	1.96	7	600
C3	He/Ar	Ar	2	1.96	14	600
C4	He/Ar	Ar	5	1.96	5	980
C5	He/Ar	Ar	5	1.96	20	980
C6	He/Ar	Ar	5	1.96	43	980
C7	N ₂	N ₂	2	1.67	1	425
C8	N ₂	N ₂	2	1.67	5	425
C9	N ₂	N ₂	2	1.67	10	425
C10	N ₂	N ₂	5	1.67	3	570
C11	N ₂	N ₂	5	1.67	12	570
C12	N ₂	N ₂	5	1.67	25	570

**Fig. 1** Conditions during a shock tube experiment (common nomenclature)

LITA measurements (i.e. x_{LITA}), different flow properties can be observed over time.

In the study, we focused on two quite different post-shock states within a shock tube experiment. LITA measurements were performed immediately after the incident shock wave (State 2 in Fig. 1), where the test gas is not only compressed and heated but also accelerated towards the end wall of the test section. Secondly, experiments after the reflected shock wave at the end wall (State 5 in Fig. 1) were carried out. Due to the double-compression, this provides a quiescent environment at high pressure and temperature.

Our objective was to create conditions at four temperature levels at different pressures, leading to the 12 cases in Table 1. This shall provide a reasonable variety of experimental conditions for validation and quantitative measurements with LITA.

To generate such conditions, we targeted a constant Mach number of the incident shock wave for each set of experiments (C1–C6 and C7–C12). It is defined by

$M_s = v_s/a_1$, with v_s the shock velocity (in laboratory coordinate system) and a_1 the speed of sound of the test gas at state 1. M_s only depends upon the driver/test gas combination and p_4/p_1 , which is the initial pressure ratio between driver (state 4) and test gas (state 1). For all cases (C1–C12), a value of $p_4/p_1 \approx 19$ was chosen.

To estimate M_s , resulting from the chosen p_4/p_1 , former calibrations of the shock tube were used [56]. For cases C1–C6 with a He/Ar mixture (≈ 80 vol%/20 vol%) as driver and test gas Ar, the nominal Mach number was $M_{s,Ar} = 1.96$. The N₂–N₂ gas combination used for cases C7–C12 leads to $M_{s,N_2} = 1.67$. Note that the actual M_s for each experiment deviates due to variations in p_4/p_1 .

Assuming ideal gas behavior for Ar and N₂, the theoretical pressure ratios $p_{i,th}/p_1$ and temperature ratios $T_{i,th}/T_1$ behind the incident ($i = 2$) and reflected ($i = 5$) shock can be calculated based on the nominal M_s using inviscid 1D shock theory [57]. We chose three different p_1 that lead to $p_{5,th}$ values in the order of 5, 20 and 43 bar (cases C4–C6) for $M_{s,Ar}$. Correspondingly, $p_{2,th}$ values of 2, 7 and 14 bar are reached (cases C1–C3). Due to a similar T_1 with $\Delta T_1 \pm 1.5$ K for all experiments, the post-shock temperatures are similar for the same M_s . For C1–C6, $T_{2,th}$ and $T_{5,th}$ are approx. 600 and 980 K. The same procedure applied to C7–C12 yields values for $p_{2,th}$ of 1, 5 and 10 bar and for $p_{5,th}$ of 3, 12 and 25 bar. $T_{2,th}$ and $T_{5,th}$ are calculated to 425 and 570 K.

2.3 Acquisition and uncertainty of experimental conditions

The pressure evolution within the test section was captured by two piezo-electric pressure sensors from Kistler (603 B) with Kistler charge amplifiers 5011 B. The axial distance between the pressure sensors was 79.5 mm. The axial measurement position of LITA (x_{LITA}) coincided with the axial position of the sensor closer to the test section end

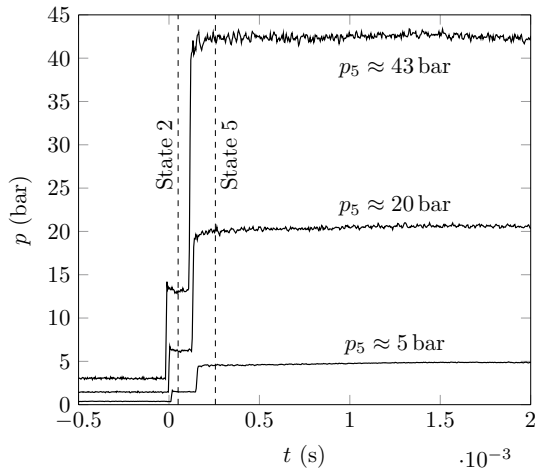


Fig. 2 Pressure traces recorded at x_{LITA} for He-Ar/Ar for $p_5 \approx 5$, 20 and 43 bar

wall, which was mounted 51.5 mm upstream of the end wall.

In Fig. 2, the experimental pressure records at x_{LITA} are exemplarily shown for the He-Ar/Ar configuration at $p_{5,exp} \approx 5$, 20 and 43 bar (i.e. C1–C3 or C4–C6). For the sake of illustration, the signals were slightly shifted in time to identify the distinct curves.

The shock velocity and $M_{s,exp}$ were calculated based on the time difference Δt_s from the arrival of the incident shock wave at the first (not depicted in Fig. 2) and second pressure sensor. It is then possible to calculate the theoretical post-shock states after incident and reflected shock based on $M_{s,exp}$. Δt_s was determined with an uncertainty of $\pm 2 \mu s$. This can be considered to be a conservative error approximation to account for uncertainties in the detection of the pressure rises and positioning of the pressure sensors. The overall error margins for the calculated values (based on $M_{s,exp}$) were determined as combination of the resulting uncertainty in $M_{s,exp}$ and the uncertainties of the initial state variables. For example, the error margin for $T_{5,th}$ was calculated with $\Delta T_{5,th} = |\partial T_{5,th}/\partial M_s| \Delta M_s + |\partial T_{5,th}/\partial T_1| \Delta T_1$. All other state variables were treated accordingly. T_1 was measured with a PT100 with $\Delta T_1 \pm 1K$, leading to maximum errors for $T_{2,th}$ and $T_{5,th}$ of 2.3 and 3.2 %. p_1 was gained from a Keller PAA-33X sensor with total absolute error band of ± 0.0025 bar. For all investigated cases, this results in a maximum relative error margin for $p_{2,th}$ and $p_{5,th}$ of 4 and 6 %, respectively. p_{exp} was extracted from the pressure trace at the time of the LITA experiment defined by the laser trigger pulse. The pressure trace was averaged over 100 μs to account for signal noise, where the uncertainty of p_{exp} was below 3 %. The aforementioned uncertainties were calculated for each particular case and are incorporated in the result section.

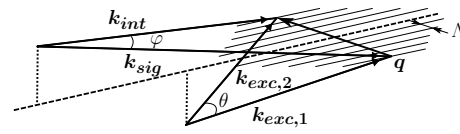


Fig. 3 Forward folded BOXCARS configuration used for phase matching

3 Laser-induced thermal acoustics

3.1 Fundamentals

For LITA, two excitation beams are crossed under an angle θ to form an ellipsoidal intensity grating in the electric field. The fringe spacing Λ is a function of θ and the excitation beam wavelength λ_{exc} , namely

$$\Lambda = \frac{\lambda_{exc}}{2 \sin(\theta/2)}. \quad (1)$$

The nonlinear response of the test medium to the electric field grating results in the formation of a density grating with the same Λ . Scattering of the interrogation beam under an incident angle φ is most efficient, if the Bragg condition

$$\frac{\lambda_{int}}{2 \sin(\varphi/2)} = \frac{\lambda_{exc}}{2 \sin(\theta/2)} = \Lambda \quad (2)$$

is fulfilled. Only then, the scattering results in a coherent signal beam. As the refractive index is approximately constant for both the excitation and interrogation wavelength ($n(\lambda_{exc}) \approx n(\lambda_{int})$), this results in a phase-matching requirement for the setup

$$\pm(\mathbf{k}_{exc,1} - \mathbf{k}_{exc,2}) = \pm(\mathbf{k}_{int} - \mathbf{k}_{sig}) = \mathbf{q}, \quad (3)$$

with $|\mathbf{q}| = 2\pi \Lambda^{-1}$, where \mathbf{k} and \mathbf{q} denote the wave vectors of the laser beams and the resulting grating. An illustration of this arrangement is shown in Fig. 3.

For a sufficiently short excitation pulse, electrostriction and thermalization, responsible for the grating formation, can be modeled as response of the test medium to an intensity pulse with Diracian time profile [18]. Electrostriction depends on the real part of the molecular susceptibility of the test gas, thermalization on the imaginary part. Hence, electrostriction relies on the polarizability of the molecules causing an movement towards or away from regions of high optical intensity. Modeled as rapid forcing of the momentum equations, it results in two conjugate acoustic wave packages, which counter-propagate normal to the plane of the grating fringes. Thermalization is caused by the absorption of light by the test medium and, hence, requires the energy equation. If the resulting heat up occurs fast, a non-propagating thermal wave is generated in addition to the propagating acoustic wave packages.

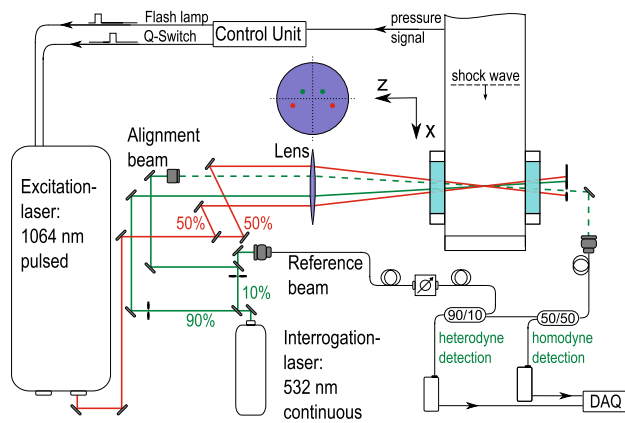


Fig. 4 Optical setup of LITA including data acquisition

The modulation of the density grating is a combination of these optoacoustic effects and a result of the constructive and destructive interference of the present waves. In these experiments, only non-resonant LITA was performed, leaving electrostriction the only grating formation mechanism. The density grating is then solely a result of the interaction of the two acoustic wave packages. The scattered, time-resolved signal beam is modulated in its intensity, which reflects the dynamic behavior of the density grating in time. The intensity of the density grating gradually reduces due to dissipative effects, which damps the oscillation of the signal beam with increasing lifetime.

For velocimetry, the homodyne detection scheme is extended by a fourth input beam. This so-called reference beam or local oscillator is introduced collinearly to the signal beam. Generally, the frequency of the homodyne signal is only a function of the speed of the acoustic wave packages relative to each other. Therefore, even if a test medium with a velocity component v_{flow} in direction of the grating vector \mathbf{q} is considered, the homodyne frequency remains unchanged¹. However, the individual acoustic wave packages now propagate with $v_- = |a - v_{\text{flow}}|$ and $v_+ = |a + v_{\text{flow}}|$, which Doppler shifts the frequency of the signal scattered from the wave packages proportional to the flow velocity. By heterodyne mixing of the reference beam with the signal beam, the beat frequencies due to Doppler shift are isolated and the flow velocity can be determined.

3.2 Optical setup

Figure 4 shows the optical arrangement used for the experiments. A pulsed Nd:YAG laser serves as excitation source (Continuum Powerlite 8010, $\lambda_{\text{exc}}=1064$ nm, $\tau_{\text{pulse}}=7$ ns

¹ Schlamp et al. [33] realized homodyne velocimetry via deliberate beam misalignments.

FWHM, 30 GHz linewidth) and is split into two excitation beams.

For an efficient grating excitation, the two beams must be equal in intensity with an optical path adaption within the coherence time of the laser [18] and polarized perpendicular to the crossing plane [58]. A continuous wave DPSS laser (Coherent Verdi V8, $\lambda_{\text{int}}=532$ nm, 5 MHz linewidth) is used as interrogation laser. All beams are arranged in a forward folded BOXCARS configuration to achieve phase matching (see Fig. 3). The beams are focused into the measurement volume by an AR-coated lens ($f = 700$ mm) at a crossing angle of $\theta = 3^\circ$. In addition, excitation and interrogation beams are slightly tilted towards each other to support spatial separation of the weak signal and strong input beams. This beam alignment results in an ellipsoidal measurement volume approximately $200 \mu\text{m}$ in diameter and about 8 mm in length. The temporal resolution is given by the signal lifetime, which is typically between 500 and 1000 ns and, hence, well below time scales of the shock tube ($\mathcal{O}(\text{ms})$ for states 2 and 5, see Fig. 2).

The scattered signal beam is spatially and spectrally filtered and directed into two avalanche detectors (Thorlabs APD110, 3 dB bandwidth 0–62.5 MHz [59]) via single-mode fibers and couplers. The signal beam is split to perform a homodyne and heterodyne signal detection simultaneously. The reference beam is split off the interrogation beam and adjusted to the signal beam intensity via a variable attenuator. An alignment beam is used to mimic the signal beam path to align the detector-side optics. The voltage signal of the detectors is recorded by a 1GHz bandwidth digital oscilloscope (LeCroy, Waverunner 104Xi).

The output power of the excitation laser remained constant at approximately 90 mJ for all experiments. The power of the interrogation laser varied from 1 to 6 W to ensure a signal-to-noise ratio greater 10 for all experimental conditions.

3.3 Signal acquisition and processing

Generally, the frequency of LITA measurements is limited to the repetition rate of the excitation laser (10 Hz by default). As the arrival of the incident shock wave is arbitrary in time, an intermediate laser pulse in between the regular pulses is required. This ensures that the measurement is always taken at the same time relative to the shock wave propagation. The required trigger logic was developed at ITLR and has been widely used in several laser diagnostic experiments. It is necessary to block an intermediate pulse—if it is too close to the regular pulse—to protect flash lamp and laser rods from damage. The repetition rate of the excitation laser was changed from 10 to 5 Hz to increase the success rate for firing a laser pulse to 95 %. A stable operation was proven through of a shot-to-shot

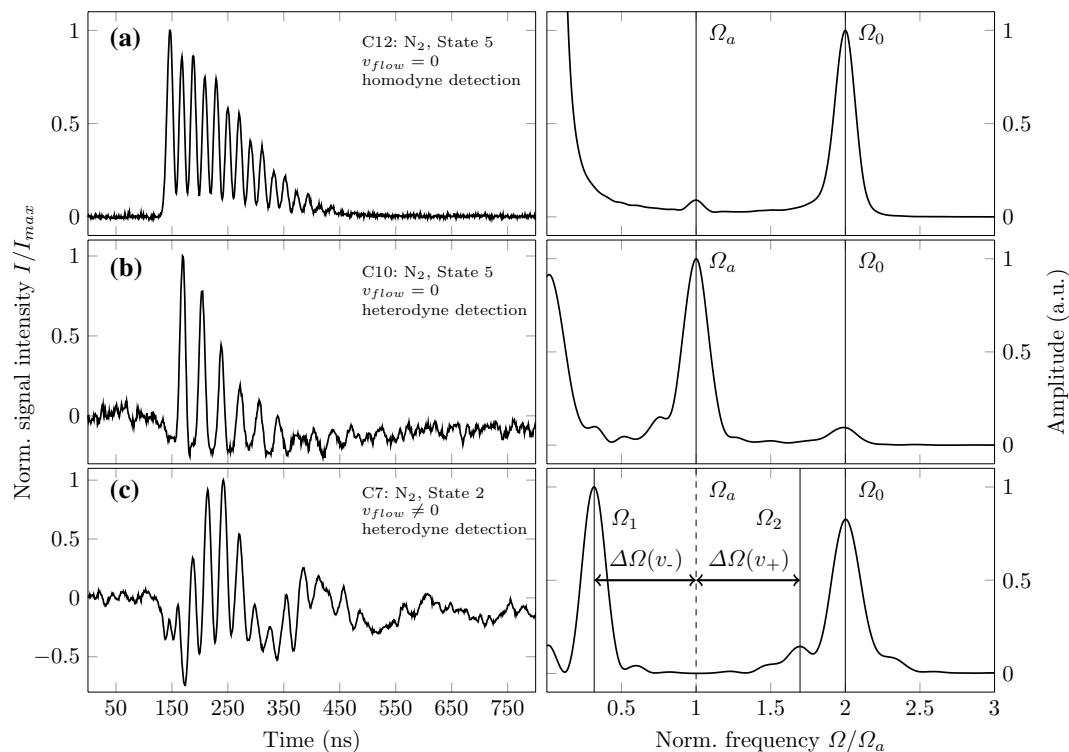


Fig. 5 Experimental LITA signals together with the corresponding frequency spectrum for different flow states

variability of the laser intensity within $\pm 5\%$. This is particularly important to avoid damaging the windows due to exceptionally high pulse intensities. The data acquisition system is triggered by a pressure transducer in the driven section far upstream of the test section end wall. LITA signals were recorded for their entire lifetime, which was typically less than one microsecond.

Generally, two processing schemes are available for LITA signals. Firstly, Cummings et al. [17] derived a theoretical model based on linearized equations of hydrodynamics and light scattering. The analysis includes finite-beam size effects and both electrostriction and thermalization. Least square curve fitting algorithm may be used to match time-resolved experimental LITA data to the theoretical model. The primary outputs are the speed of sound, flow velocity and transport properties of the test gas.

Secondly, a spectral analysis of the recorded signal can be performed to extract the speed of sound and the flow velocity. This approach has been chosen for this study in form of a Fourier transformation of the time-resolved signal. The influence of the detection scheme and flow state is illustrated in Fig. 5 showing three recorded LITA signals for N_2 together with the corresponding frequency spectra.

For purely non-resonant LITA, the intensity of the homodyne signal in Fig. 5a is modulated only at the frequency $\Omega_0 = 2\Omega_a$ as each acoustic wave package travels at the speed of sound, but in opposite direction resulting in

propagation velocity of twice the speed of sound relative to each other. By using Λ as the wavelength of the two counter-propagating acoustic waves, the speed of sound can be calculated from

$$a = \frac{\Omega_0 \Lambda}{2} = \Omega_a \Lambda. \quad (4)$$

If the test gas composition is known, the temperature may also be derived for a given equation of state. For an ideal gas, it is

$$T = \frac{a^2}{\gamma R}. \quad (5)$$

For given speed of sound at a priori unknown temperature, $\gamma(T, p)$ was found through an iterative procedure using the property database NIST REFPROP. This procedure inherently assumes thermodynamic equilibrium. Note that for N_2 at high temperatures, non-equilibrium processes due to vibrational relaxation can be considerable preventing the determination of temperature from Eq. 5. For all temperatures of the investigated N_2 cases (C7–C12), this contribution is considered low enough [60] to justify the chosen approach. The fringe spacing Λ can be found prior via a calibration measurement at known speed of sound (see Sect. 4.1).

Heterodyne detection allows to resolve the frequency shift of the light being scattered from the moving acoustic wave packages. For quiescent test gas as in Fig. 5b,

the corresponding spectrum shows a beat frequency at Ω_a in addition to $\Omega_0 = 2\Omega_a$. Ω_0 is only a function of the relative speed as it is also the case for homodyne detection. Ω_a results from the mixing with the reference beam, which is not scattered from a moving source and hence is not shifted. As a consequence, the beat frequency at Ω_a relates to the absolute velocity of the wave packages. If a test medium with a velocity component v_{flow} in direction of the grating vector \mathbf{q} is considered (Fig. 5c), the wave packages then travel at $v_- = |a - v_{\text{flow}}|$ and $v_+ = |a + v_{\text{flow}}|$. The spectrum shows that Ω_a splits symmetrically into two beat frequencies at $\Omega_1 = \Omega_a - \Delta\Omega(v_{\text{flow}})$ and $\Omega_2 = \Omega_a + \Delta\Omega(v_{\text{flow}})$, resulting from the different propagation speed of the individual wave packages. Ω_0 remains unchanged as the relative speed is still the same.

For subsonic post-shock flows², the velocity and Mach number M_{flow} can be calculated from the beat frequencies using

$$|v_{\text{flow}}| = \frac{\Omega_2 - \Omega_1}{2} \Lambda \quad (6)$$

and

$$M_{\text{flow}} = \frac{\Omega_2 - \Omega_1}{\Omega_2 + \Omega_1}. \quad (7)$$

Note that M_{flow} can be found independently from Λ .

The oscilloscope temporally discretizes the signals with 0.1-ns time steps which results typically in 300 data points for a single oscillation at Ω_0 of the LITA signals. As can be seen in Fig. 5, clear peaks are formed in the spectrum at the characteristic frequencies. Hence, manual selection of the peaks is seen sufficient to extract the relevant frequencies for conversion into flow quantities. The errors solely from the uncertainty of the peak determination are 0.1 and 0.4 % for speed of sound and flow velocity, respectively. This contribution, however, is small compared to the overall uncertainty of analyzing LITA signals using a Fourier transform. A detailed study of signal analysis algorithms for LITA signals was performed by Balla and Miller [61]. Here, a relative standard deviation in frequency of 1.7 % was obtained for a FFT based algorithm.

4 Results

4.1 Setup calibration

For all experiments, the fringe spacing Λ was found from calibration in ambient air with a speed of sound determined

² An analog dependency can be found for supersonic flows by taking into account that both wave packages then travel in the same direction as the fluid.

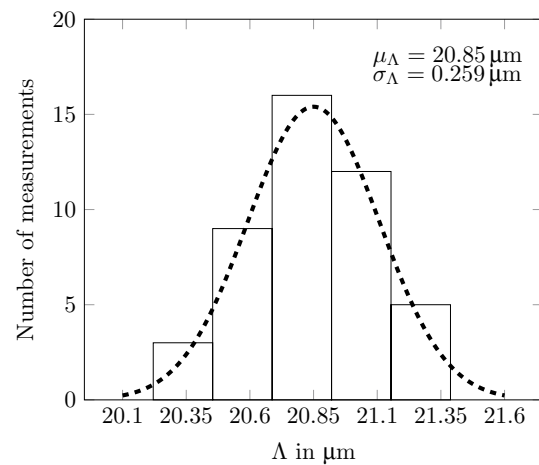


Fig. 6 Frequency distribution of fringe spacings determined from measured Ω_0 of 50 LITA signals

from a temperature measurement and Eq. 4. Here, 50 homodyne signals were recorded. Figure 6 shows the resulting fringe spacing based on the measured frequency Ω_0 .

The spacing has a normal distribution with an expected value of $\mu_\Lambda = 20.85 \mu\text{m}$ and a standard deviation $\sigma_\Lambda = 0.259 \mu\text{m}$, resulting in a relative standard deviation $\sigma_\Lambda/\mu_\Lambda = 1.24 \%$.

This gives a first impression of the setup's precision, which is within the expected uncertainty for a frequency analysis using a fast Fourier transformation for a damped oscillation [61]. A second calibration was carried out after 10 shock experiments. The relative deviation of the fringe spacings between both calibrations was below 0.5 %. The systematic error is considered to be small compared to the uncertainty of single-shot measurements due to the shown precision. This proves the optical setup being sufficiently robust against external influences. Note that Λ can also be found without a calibration using Eq. 1. θ is then calculated by a trigonometric function using the distance of the beams and the focal length of the lens. For the presented setup, this yields $\Lambda = 20.4 \mu\text{m}$. Hence, the setup can be regarded calibration-free, if a systematic error of about 3 % is acceptable.

4.2 Precision and accuracy analysis

We verified the reproducibility for real test environments by six experiments at the same conditions to evaluate precision and accuracy of LITA. Note, however, that an accurate statistical analysis would require more experiments (typically 20 or more). Based on an analysis of Gurland and Tripathi [62], we chose six measurements as a good compromise between accuracy and experimental effort. Hence, the

derived standard deviations and 95 % confidence intervals are merely an estimate.

The analysis was carried out for two representative conditions, where the lowest signal-to-noise ratios (SNR) were expected. Generally, it is the case for low-pressure and high-temperature conditions. Therefore, condition C7 (lowest pressure) and C4 (lowest pressure at highest temperature) were selected. Note that C7 represents state 2 with

N_2 as test gas, while for C4 state 5 in Ar was investigated. Examples of recorded LITA signals at these conditions are illustrated in both Fig. 5 and Fig. 10.

Figure 7 shows six C7 experiments, where M_2 and a_2 were simultaneously measured. T_2 was derived from a_2 according to Eq. 5.

Single-shot precision of $M_{2,meas}$ and $a_{2,meas}$ yield relative standard deviations below 1.7 %. This is reasonably close to the value found for the calibration measurement in Sect. 4.1, indicating a sufficient precision for real conditions. The value doubles for $T_{2,meas}$ to 3.4 %. due to error propagation. Figure 7 also holds the theoretical values calculated based on $M_{s,exp}$, including error bars according to Sect. 2.3. It can be deduced that the experimental conditions feature high reproducibility and, therefore, provide a good validation basis for the measured values. Relative deviations for the averaged values $\delta\bar{x}_i = (\bar{x}_{meas} - \bar{x}_{th})/\bar{x}_{th}$ of M_2 , a_2 and T_2 are +0.35, +0.04 and +0.19 %, respectively. This proves that the uncertainty of a single-shot measurement is dominated by random rather than systematic errors.

In Fig. 8, a_5 and T_5 for the reflected shock case (C4) are illustrated. Experiments 1 to 6 yield relative standard deviations for $a_{5,meas}$ and $T_{5,meas}$ of 1.3 and 2.7 %, which is comparable to the precision of the incident shock case and the calibration. However, we found a discrepancy of measured and theoretical values up to $\delta_{a_5} = -2.8\%$ and $\delta_{T_5} = -5.9\%$. Figure 9 shows the pressure trace for a typical C4 experiment.

The data for experiments 1–6 were taken 161 μs after the reflected shock pass-by. As $p_{5,th}$ is not reached until approx.

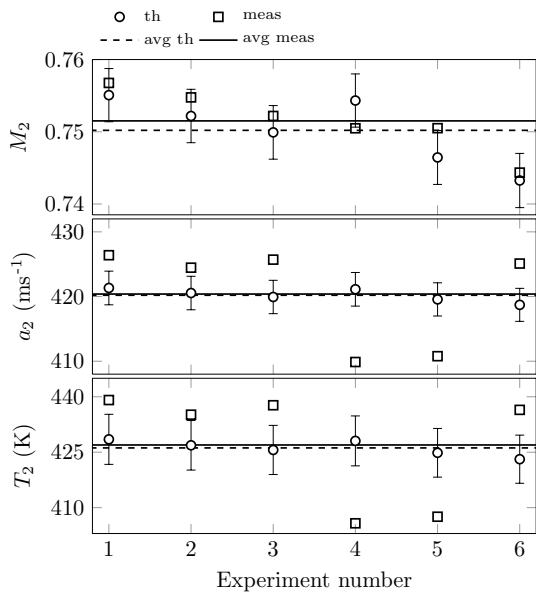


Fig. 7 Theoretical (th) and measured (meas) M_2 , a_2 and T_2 for six experiments at condition C7

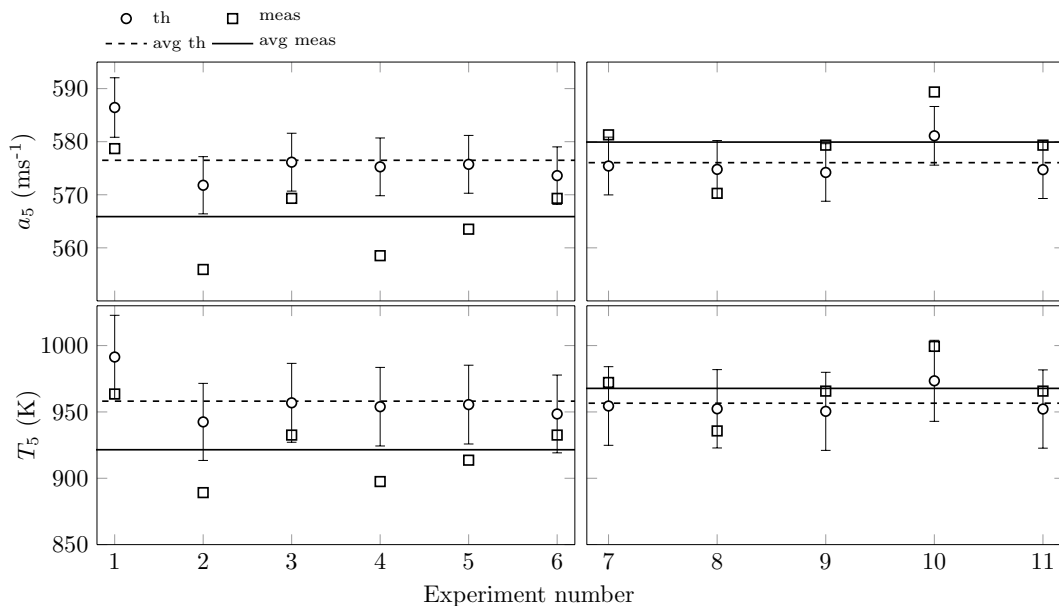


Fig. 8 Theoretical (th) and measured (meas) a_5 and T_5 for experiments at condition C4

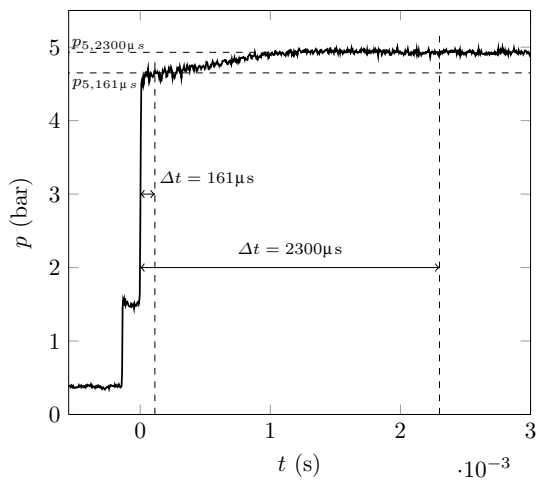


Fig. 9 Pressure trace for typical C4 experiment and chosen measurement positions for accuracy analysis

Table 2 Summary of precision analysis

	$\overline{M}_{2,meas}$ (-)	\overline{T}_{meas} (K)	$\sigma_{M_{2,meas}}$ (-)	$\sigma_{T,meas}$ (K)
C7	0.750	427.0	0.0078	14.4
C4	-	921.5	-	24.8

1 ms after the shock pass-by, we expect $a_{5,meas} < a_{5,th}$ and $T_{5,meas} < T_{5,th}$. Therefore, a second set of measurements (7–11) was obtained at 2300 μ s where $p_{5,th} \approx p_{5,exp}$. For these measurements, the maximum δ_{a_5} and δ_{T_5} reduce to 1.4 and 2.7 %, while the precision of 2.1 % in temperature is comparable to the first set. The discrepancies between averaged temperatures reduce from $\delta_{\overline{T}_5} = -3.8\%$ at 161 μ s to $\delta_{\overline{T}_5} = 1.1\%$ at 2300 μ s. As the discrepancy is mutually found for both temperature and pressure in the first set together with this consistent trend, we attribute this as a feature of non-idealities rather than a systematic error in LITA. Furthermore, Farooq et al. [13] showed that a change in state as it is observed between 161 μ s and 2300 μ s should follow an isentropic relation. This isentropic change can be approximated, for instance using the averages of measured pressure and temperature, i.e.

$$0.97 = \left(\frac{\overline{p}_{meas,161\mu s}}{\overline{p}_{meas,2300\mu s}} \right)^{\frac{(\gamma-1)}{\gamma}} \approx \frac{\overline{T}_{meas,161\mu s}}{\overline{T}_{meas,2300\mu s}} = 0.96. \quad (8)$$

Table 2 summarizes \overline{T}_{meas} and $\overline{M}_{2,meas}$ together with σ of the determined quantities. Experiments 1–6 were used for the C4 case. It is concluded that the post-processing using a FFT is the major source of uncertainty as the values found for the calibration and the test cases are close to the

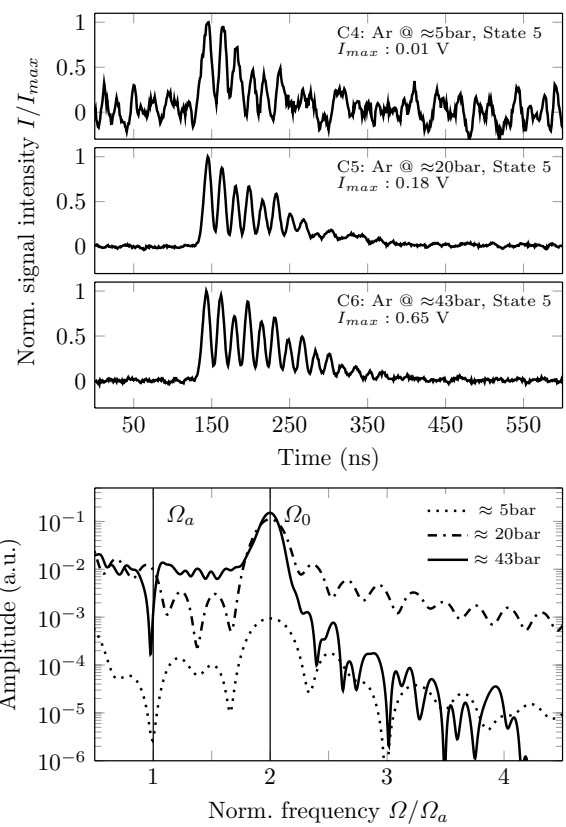


Fig. 10 Experimental LITA signals taken after reflected shock for constant $T_5 \approx 980$ K and different pressures p_5

uncertainty in frequency determination reported by Balla and Miller [61].

The investigation proves that the setup is sufficiently robust for the use in the shock tube. For following analysis, we use the derived relative standard deviations to estimate a corresponding 95 % confidence interval. It is a conservative error estimation for two reasons. Firstly, the SNR of cases C4 and C7 are around ten and the lowest in the entire campaign, but increases with pressure. Secondly, the signal lifetime also prolongs with increasing pressure resulting in a higher number of oscillations. This is illustrated in Fig. 10 showing three LITA signals for Ar (C4–C6) at different pressures. For the highest pressure, the SNR improves significantly to values of up to 100. Furthermore, the frequency spectrum shows that a more defined peak at Ω_0 is formed for an increased number of oscillations.

4.3 Case analysis

To comprehensively demonstrate LITA for typical shock tube conditions, all cases in Table 1 were investigated. Table 3 contains a detailed summary of all measured values including their corresponding theoretical values and the relative deviation of both. Furthermore, $M_{s,exp}$ and p_{exp} are

included. Examples of experimental LITA signals for half of those conditions are incorporated in Fig. 5 and Fig. 10 to give an impression of the obtained signals.

For the following considerations, we put a focus on T_{meas} and M_{meas} with corresponding theoretical values. In Fig. 11, T_2 (C1–C3; C7–C9) and T_5 (C4–C6; C10–C12) are shown. To visualize the distinction between T_2 and T_5 , a dashed line shall symbolize the two different temperature (i.e. pressure) levels in state 2 and 5. For this, the design values from Table 1 were used. The Ar cases C1–C6 are contained in the left plot, and C7–C12 with N₂ can be found in the right part. In the lower plots, δ is presented for each condition.

Due to the different pressure levels and, therefore, varying sensitivity of p_4/p_1 to small inaccuracies in the target filling pressures, the $M_{s,\text{exp}}$ deviate slightly from their design values (see Table 1). However, the T_{th} still match the design values quite well, especially considering the uncertainty determined in Sect. 2.3. Hence, it is valid to compare them to our T_{meas} gained from LITA for a quality assessment.

Figure 11 shows that in all 12 cases T_{th} lies within the 95 % confidence interval of T_{meas} symbolized with the error bars. This suggests that T_{meas} was determined with good accuracy for all pressure and temperature levels. The maximum δ_{T_2} is found at C3 (Ar @ ≈ 13 bar) with -4.8% , where C12 (N₂ @ ≈ 24 bar) shows the maximum δ_{T_5} of 3.7% .

Generally, we found a tendency of too low T_{meas} compared to T_{th} (especially for C2–C6). Despite the uncertainty due to the single-shot measurements (i.e. frequency analysis), this may be found in the discrepancy between p_{th} and p_{exp} (see also Fig. 9) caused by non-ideal effects. In all cases p_{exp} is smaller than p_{th} , which inevitably leads to lower T_{meas} . This leads to the conclusion that the actual magnitude of δ_T (and also δ_M) is an interplay between both the LITA measurement uncertainty and the inaccuracy of thermodynamic state value prediction. More importantly, the expected value in all cases stays within the 95 % confidence interval of measurement based on the precision found in Sect. 4.2. $M_{2,\text{meas}}$ shows very good agreement

Table 3 Summary of results for cases C1–C12 from Table 1

Case	$M_{s,\text{exp}}$	p_{th} (bar)	p_{exp} (bar)	$M_{2,\text{th}}$ (–)	$M_{2,\text{meas}}$ (–)	a_{th} (ms^{-1})	a_{meas} (ms^{-1})	T_{th} (K)	T_{meas} (K)	δ_M (%)	δ_a (K)	δ_T (K)
C1	1.958 ± 0.030	1.6	1.4	0.763	0.764	456.2	458.8	600.0	605.5	0.14	0.56	0.92
C2	1.980 ± 0.031	6.8	6.3	0.770	0.763	459.2	452.8	607.9	590.0	-0.97	-1.39	-2.95
C3	1.984 ± 0.031	14.2	13.2	0.770	0.761	460.6	449.8	611.4	582.0	-1.11	-2.34	-4.80
C4	1.972 ± 0.031	5.1	4.8	–	–	586.4	578.7	991.4	963.5	–	-1.32	-2.81
C5	1.971 ± 0.031	20.6	20.4	–	–	586.9	583.8	992.9	980.6	–	-0.53	-1.24
C6	1.973 ± 0.031	43.5	41.7	–	–	588.9	587.1	999.5	991.7	–	-0.30	-0.77
C7	1.681 ± 0.025	1.1	1.1	0.754	0.760	420.5	424.5	426.9	435.1	0.68	0.93	1.94
C8	1.658 ± 0.024	4.4	4.2	0.735	0.725	418.4	417.0	422.4	419.9	-1.37	-0.34	-0.59
C9	1.672 ± 0.024	9.4	9.0	0.745	0.743	420.2	422.0	426.2	430.0	-0.24	0.41	0.90
C10	1.665 ± 0.024	2.9	2.8	–	–	483.9	477.3	569.9	550.2	–	-1.37	-3.45
C11	1.666 ± 0.024	11.7	11.6	–	–	484.8	488.4	571.9	576.2	–	0.76	0.77
C12	1.671 ± 0.024	24.4	24.4	–	–	486.4	497.1	575.9	596.9	–	2.20	3.66

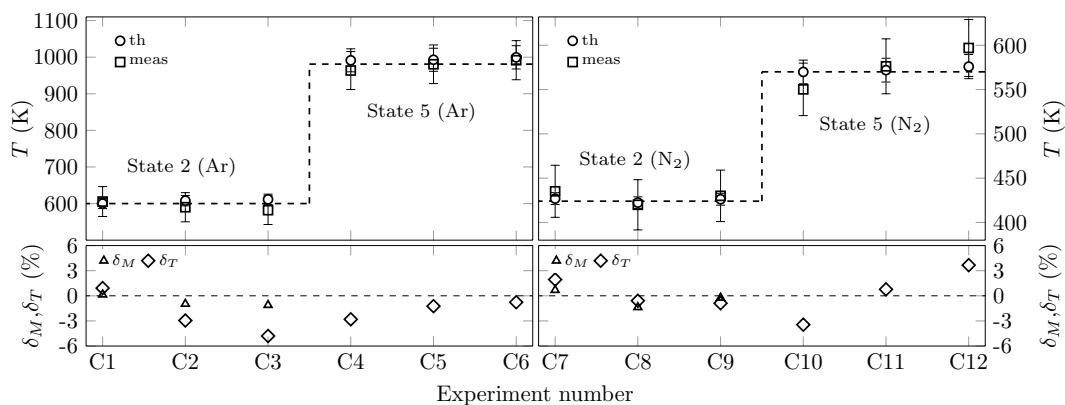


Fig. 11 T_{meas} and T_{th} for cases C1–C12 including δ_T and δ_M

with $M_{2,\text{th}}$ for all cases. A maximum δ_{M_2} (Δ) is found for case C8 with $\delta_{M_2} = -1.4\%$. The above comparison proves the reliability of LITA to accurately determine temperature (i.e. speed of sound) and Mach number of shock-heated flows.

Given that signals were recorded for a range of pressures and temperatures, we derived the influence of both quantities on the LITA signal intensity. To allow for a meaningful comparison, all signals were scaled with respect to the intensities of the input beams. The upper part of Fig. 12 shows the amplitude of the first LITA oscillation for each signal. Generally, the LITA intensity at a constant temperature significantly increases with higher pressures. A quadratic fit of the form $c(T)p^2$ (solid lines) shows good agreement (R-squared >0.98) with the experimental data. This square-dependency on pressure has already been reported by Cummings [63]. The coefficients $c(T)$ represent the temperature dependency. In the lower part of Fig. 12, $c(T)$ of each fit is plotted versus temperature. Similar to the approach for the pressure dependency, a power function represents a good approximation of the experimental data. Danehy [64] reported a

T^{-3} dependency for electrostrictive gratings in quiescent test gas, while Schlamp et al. [55] found $T^{-4.25}$ for non-resonant LITA measurements in a supersonic free jet. For our experiments, signal intensity scales with $T^{-3.4}$, which is in between the reported values.

The found $p^2T^{-3.4}$ dependency is seen as estimate for the applicability of LITA at experimental conditions other than those investigated here. It further demonstrates the potential to include pressure measurements using LITA. For quantitative pressure measurements, however, more detailed experiments with respect to the pressure dependency must be conducted to quantify parasitic effects on the measurements such as stray light.

5 Conclusion

The capabilities of single-shot laser-induced thermal acoustics (LITA) for shock-heated flows was assessed in a comprehensive study using a shock tube. Speed of sound, temperature, velocity and Mach numbers were determined for the subsonic flow behind the incident shock and the quiescent gas after the reflected shock wave for argon and nitrogen as test gases. Calibration measurements of the fringe spacing showed a Gaussian distribution with a relative standard deviation of 1.2%. The robustness of the setup toward external influences was proven by means of a second calibration run after several experiments yielding comparable values. Hence, systematic error in the fringe spacing calibration was negligible.

We performed a precision and accuracy analysis using a representative condition after incident ($T_2 \approx 425\text{ K}$, $p_2 \approx 1\text{ bar}$) and reflected shock ($T_5 \approx 980\text{ K}$, $p_5 \approx 5\text{ bar}$) with low signal-to-noise ratios of around 10. For each case, multiple experiments at the same conditions were carried out to allow for statistical analysis. After the incident shock wave, this yielded a single-shot precision for temperature and Mach number of 3.4 and 1%. Theoretical values based on 1D inviscid shock wave theory were used for accuracy estimation. The averages of measured and calculated values showed relative deviations $<0.35\%$ for both T and M .

For the reflected shock case, a single-shot precision of 2.7% in the post-shock temperature was found for the measured data. In this case, non-idealities lead to a discrepancy of -3.8% for the averages of calculated and measured values. A second set of experiments taken at a larger time after the shock passage yielded a deviation in average temperatures of 1.15%. As a consequence, the precision and accuracy of single-shot LITA measurements are proven to be well sufficient even for worst-case scenarios. The found performance reaches up to what is reported for more established techniques such as LIF and CARS, but in its present state stays behind high-accuracy, time-resolved TDLAS

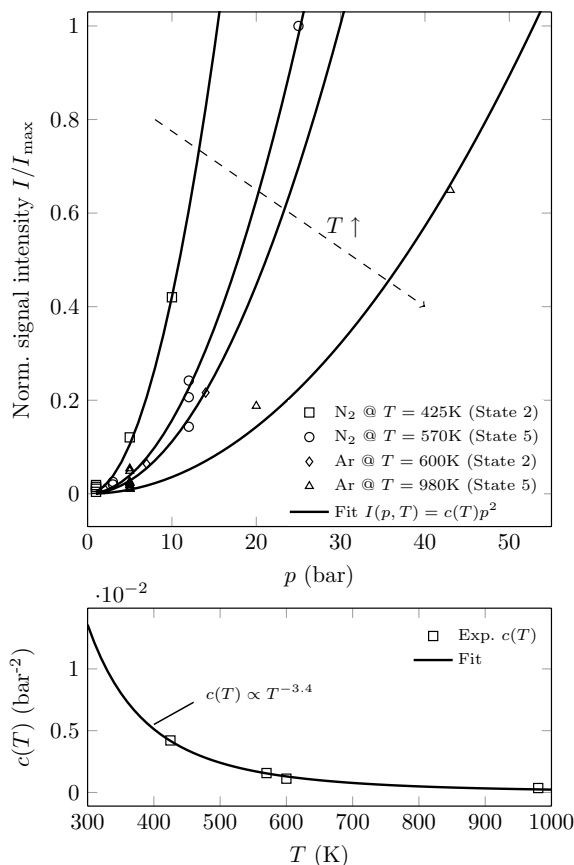


Fig. 12 Dependency of LITA signal intensity on pressure and temperature

systems. For future experiments, precision will be improved using more sophisticated post-processing algorithms based on theoretical models for the LITA signal generation.

We further investigated 12 conditions with pressures from 1–43 bar and temperatures between 420–1000 K. In all experiments, the prediction from theory was well within the 95 % confidence interval of the LITA measurement. For all cases, the maximum deviation of measured and theoretical temperatures was 4.8 %. Mach number yielded the best agreement of all measured parameters with deviations below 1.4 %. It was found that these discrepancies are an interplay between single-shot uncertainty of LITA and the inaccuracy of the theoretical state prediction. For the given range of experimental conditions, the effect of pressure and temperature on the signal intensities was investigated. Good agreement was found for a $p^2T^{-3.4}$ dependency, which allows to estimate the performance for the current setup at other conditions.

Finally it should be stated that the study evidently proves a valid applicability of LITA for shock-heated flows, especially in terms of shock tube experiments.

Acknowledgments This work was performed within the framework of the Transregio 40 “Technological foundations for the design of thermally and mechanically highly loaded components of future space transportation systems” and the GRK 1095/2 “Aero-Thermodynamic Design of a SCRamjet Propulsion System for Future Space Transportation Systems.” The authors would like to thank the German Research Foundation (DFG) for the financial support.

References

1. K. Itoh, S. Ueda, H. Tanno, T. Komuro, K. Sato, *Shock Waves* **12**, 93 (2002). doi:10.1007/s00193-002-0147-0
2. R.K. Hanson, D.F. Davidson, *Prog. Energy Combust.* **44**, 103 (2014). doi:10.1016/j.peccs.2014.05.001
3. S. Baab, G. Lamanna, B. Weigand, in *26th ILASS Americas in Portland, OR, USA, 2014* (2014)
4. R. Hruschka, S. O’Byrne, H. Kleine, *Exp. Fluids* **51**, 407 (2011). doi:10.1007/s00348-011-1039-9
5. K.J. Irimpan, N. Mannil, H. Arya, V. Menezes, *Measurement* **61**, 291 (2014). doi:10.1016/j.measurement.2014.10.056
6. J.T.C. Liu, J.B. Jeffries, R.K. Hanson, *Appl. Phys. B* **78**, 503 (2004). doi:10.1007/s00340-003-1380-7
7. A. Farooq, J.B. Jeffries, R.K. Hanson, *Appl. Phys. B* **90**, 619 (2008). doi:10.1007/s00340-007-2925-y
8. B.K. McMillin, M.P. Lee, R.K. Hanson, *AIAA J.* **30**, 436 (1992)
9. J. Yoo, D. Mitchell, D.F. Davidson, R.K. Hanson, *Exp. Fluids* **49**, 751 (2010). doi:10.1007/s00348-010-0876-2
10. S. Zabeti, A. Drakon, S. Faust, T. Dreier, O. Welz, M. Fikri, C. Schulz, *Appl. Phys. B* **118**, 295 (2015). doi:10.1007/s00340-014-5986-8
11. D.R.N. Pulford, D.S. Newman, A.F.P. Houwing, R.J. Sandeman, *Shock Waves* **4**, 119 (1994)
12. W.R. Lempert, I.V. Adamovich, *J. Phys. D: Appl. Phys.* **47**, 26 (2014). doi:10.1088/0022-3727/47/43/433001
13. A. Farooq, J.B. Jeffries, R.K. Hanson, *Appl. Phys. B* **96**, 161 (2009). doi:10.1007/s00340-009-3446-7
14. T. Seeger, A. Leipertz, *Appl. Opt.* **35**(15), 2665 (1996). doi:10.1364/AO.35.002665
15. A. Dreizler, T. Dreier, J. Wolfrum, *Chem. Phys. Lett.* **233**, 525 (1995)
16. P.H. Paul, R.L. Farrow, *J. Opt. Soc. Am. B* **12**, 384 (1995)
17. E.B. Cummings, I.A. Leyva, H.G. Hornung, *Appl. Opt.* **34**, 3290 (1995)
18. A. Stampanoni-Panariello, D.N. Kozlov, P.P. Radi, B. Hemmerling, *Appl. Phys. B* **81**, 101 (2005). doi:10.1007/s00340-005-1825-z
19. E.B. Cummings, *Opt. Lett.* **19**, 1361 (1994)
20. W. Hubschmid, R. Bombach, B. Hemmerling, A. Stampanoni-Panariello, *Appl. Phys. B* **62**, 103 (1996)
21. R.C. Hart, R.J. Balla, G.C. Herring, *Appl. Opt.* **38**, 577–584 (1999)
22. R. Stevens, P. Ewart, *Appl. Phys. B* **78**, 111 (2004). doi:10.1007/s00340-003-1282-8
23. D.N. Kozlov, *Appl. Phys. B* **80**, 377 (2005). doi:10.1007/s00340-004-1720-2
24. E.B. Cummings, H.G. Hornung, M.S. Brown, P.A. DeBarber, *Opt. Lett.* **20**, 1577 (1995)
25. S. Schlamp, H.G. Hornung, T.H. Sobota, E.B. Cummings, *Appl. Opt.* **39**(30), 5477 (2000). doi:10.1364/AO.39.005477
26. Y. Li, W.L. Romperts, M.S. Brown, *AIAA J.* **40**(6), 1071 (2002). doi:10.2514/2.1790
27. Y. Li, W.L. Roberts, M.S. Brown, J.R. Gord, *Exp. Fluids* **39**, 687 (2005). doi:10.1007/s00348-005-1012-6
28. S. Schlamp, T.H. Sobota, *Exp. Fluids* **32**, 683 (2002). doi:10.1007/s00348-002-0419-6
29. J. Kiefer, D.N. Kozlov, T. Seeger, A. Leipertz, *J. Raman Spectrosc.* **39**, 711 (2008). doi:10.1002/jrs.1965
30. B. Roshani, A. Flügel, I. Schmitz, D.N. Kozlov, T. Seeger, L. Zigan, J. Kiefer, A. Leipertz, *J. Raman Spectrosc.* **44**, 1356 (2013). doi:10.1002/jrs.4315
31. R.C. Hart, G.C. Herring, R.J. Balla, *Opt. Lett.* **32**, 1689 (2007)
32. H. Latzel, A. Dreizler, T. Dreier, J. Heinze, M. Dillmann, W. Stricker, G.M. Lloyd, P. Ewart, *Appl. Phys. B* **67**, 667 (1998)
33. S. Schlamp, E. Allen-Bradley, in *38th Aerospace Sciences Meeting & Exhibit* (2000)
34. M. Neracher, W. Hubschmid, *Appl. Phys. B* **79**, 783 (2004). doi:10.1007/s00340-0014-1632-1
35. C. Frazier, M. Lamnaouer, E. Divo, A. Kassab, E. Petersen, *Shock Waves* **21**, 1 (2011). doi:10.1007/s00193-010-0282-y
36. J. Jonuscheit, A. Thumann, M. Schenk, T. Seeger, A. Leipertz, *Opt. Lett.* **21**, 1532 (1996)
37. R. Stevens, P. Ewart, *Opt. Lett.* **31**, 1055 (2006). doi:10.1364/OL.31.001055
38. H. Li, A. Farooq, J.B. Jeffries, R.K. Hanson, *Appl. Phys. B* **89**, 407 (2007). doi:10.1007/s00340-007-2781-9
39. M. Lackner, G. Totschnig, F. Winter, M. Ortsiefer, M.C. Amann, R. Shau, J. Roskopf, *Meas. Sci. Technol.* **14**, 101 (2003). doi:10.1088/0957-0233/14/1/315
40. P. Wu, W.R. Lempert, R.B. Miles, *AIAA J.* **38**(4), 672 (2000). doi:10.2514/2.1009
41. B. Thurow, N. Jiang, M. Samimy, W.R. Lempert, *Appl. Opt.* **43**(20), 5064 (2004). doi:10.1364/AO.43.005064
42. W.D. Kulatilaka, J.R. Gord, S. Roy, *Appl. Phys. B* **116**, 7 (2014). doi:10.1007/s00340-014-5845-7
43. P.J. Trunk, I. Boxx, C. Heeger, W. Meier, B. Böhm, A. Dreizler, *P. Combust. Inst.* **34**, 3565 (2013). doi:10.1016/j.proci.2012.06.025
44. J.D. Miller, S. Roy, M.N. Slipchenko, J.R. Gord, T.R. Meyer, *Opt. Express* **19**(16), 15627 (2011). doi:10.1364/OE.19.015627
45. S.P. Kearney, D.J. Scoglietti, C.J. Kliewer, *Opt. Express* **21**(10), 12327 (2013). doi:10.1364/OE.21.012327
46. S. O’Byrne, P.M. Danahy, S.A. Tedder, A.D. Cutler, *AIAA J.* **45**, 922 (2007). doi:10.2514/1.26768

47. B. Hiller, R.K. Hanson, *Appl. Opt.* **27**(1), 33 (1988). doi:[10.1364/AO.27.000033](https://doi.org/10.1364/AO.27.000033)
48. A.D. Cutler, G. Magnotti, *J. Raman Spectrosc.* **42**, 1949 (2011). doi:[10.1002/jrs.2948](https://doi.org/10.1002/jrs.2948)
49. B. Hemmerling, M. Neracher, D. Kozlov, W. Kwan, R. Stark, D. Klimenko, W. Clauss, M. Oschwald, *J Raman Spectrosc* **33**, 912 (2002). doi:[10.1002/jrs.946](https://doi.org/10.1002/jrs.946)
50. B. Williams, M. Edwards, R. Stone, J. Williams, P. Ewart, *Combust. Flame* **161**, 270 (2014). doi:[10.1016/j.combustflame.2013.07.018](https://doi.org/10.1016/j.combustflame.2013.07.018)
51. F.J. Förster, B. Weigand, in *19th AIAA Hypersonics in Atlanta*, vol. 2014 (GE, USA, 2014)
52. G. C.Herring, F. Meyers, R.C. Hart, *Meas. Sci. Technol.* **20** (2009). doi:[10.1088/0957-0233/20/4/045304](https://doi.org/10.1088/0957-0233/20/4/045304)
53. T. Mizukaki, T. Matsuzawa, *Shock Waves* **19**, 361 (2009). doi:[10.1007/s00193-009-028-6](https://doi.org/10.1007/s00193-009-028-6)
54. T. Sander, P. Altenhoefer, C. Mundt, *AIAA J.* (2015). doi:[10.2514/1.T4556](https://doi.org/10.2514/1.T4556)
55. S. Schlamp, T. Rösgen, D.N. Kozlov, C. Rakut, P. Kasal, J. von Wolfersdorf, *J. Propul. Power* **21**, 1008 (2005)
56. I. Stotz, G. Lamanna, H. Hettrich, B. Weigand, *Rev. Sci. Instrum.* **79** (2008). doi:[10.1063/1.3058609](https://doi.org/10.1063/1.3058609)
57. H. Oertel, *Stossrohre* (Springer, New York, 1966)
58. S. Rozouvan, T. Dreier, *Opt. Lett.* **24**(22), 1596 (1999). doi:[10.1364/OL.24.001596](https://doi.org/10.1364/OL.24.001596)
59. Thorlabs, *APD110x Series Avalanche Photodetectors* (2011)
60. R. Fowler, E. Guggenheim, *Statistical Thermodynamics* (Cambridge University Press, Cambridge, 1960)
61. R.J. Balla, C.A. Miller, Nasa TechReport 2008-215327 (2008)
62. J. Gurland, R.C. Tripathi, *Am. Stat.* **25**(4), 30 (1971)
63. E. Cummings, *Laser-induced thermal acoustics*. Ph.D. thesis, California Institute of Technology (1995)
64. P. Danehy, *Population- and thermal-grating contributions to degenerate four-wave mixing*. Ph.D. thesis, Dept. of Mech.Eng., Stanford Univ. (1995)